Time Evolution of the Synchrotron X-Ray Emission in Kepler's Supernova Remnant: The Effects of Turbulence and Shock Velocity

Vincenzo Sapienza[1,2] , Marco Miceli[1,2] , Oleh Petruk[2,3,4] , Aya Bamba[5,6,7] , Satoru Katsuda[8] , Salvatore Orlando[2] , Fabrizio Bocchino[2] , and Tracey DeLaney[9]

[1] Dipartimento di Fisica e Chimica E. Segrè, Università degli Studi di Palermo, Piazza del Parlamento 1, 90134, Palermo, Italy
[2] INAF—Osservatorio Astronomico di Palermo, Piazza del Parlamento 1, 90134, Palermo, Italy
[3] Institute for Applied Problems in Mechanics and Mathematics, Naukova Street 3-b, 79060 Lviv, Ukraine
[4] Astronomical Observatory, Ivan Franko National University of Lviv, Kyryla i Methodia Street 8, UA-79005 Lviv, Ukraine
[5] Department of Physics, Graduate School of Science, The University of Tokyo, 7-3-1 Hongo, Bunkyo-ku, Tokyo 113-0033, Japan
[6] Research Center for the Early Universe, School of Science, The University of Tokyo, 7-3-1 Hongo, Bunkyo-ku, Tokyo 113-0033, Japan
[7] Trans-Scale Quantum Science Institute, The University of Tokyo, 7-3-1 Hongo, Bunkyo-ku, Tokyo 113-0033, Japan
[8] Graduate School of Science and Engineering, Saitama University, 255 Simo-Ohkubo, Sakura-ku, Saitama city, Saitama, 338-8570, Japan
[9] Physics and Engineering Department, West Virginia Wesleyan College, Buckhannon, WV 26201, USA

Abstract

The maximum energy of electrons in supernova remnant (SNR) shocks is typically limited by radiative losses, where the synchrotron cooling time equals the acceleration time. The low speed of shocks in a dense medium increases the acceleration time, leading to lower maximum electron energies and fainter X-ray emissions. However, in Kepler's SNR, an enhanced electron acceleration, which proceeds close to the Bohm limit, occurs in the north of its shell, where the shock is slowed by a dense circumstellar medium (CSM). To investigate whether this scenario still holds at smaller scales, we analyzed the temporal evolution of the X-ray synchrotron flux in filamentary structures using the two deepest Chandra/ACIS X-ray observations, performed in 2006 and 2014. We examined spectra from different filaments, measured their proper motion, and calculated the acceleration to synchrotron timescale ratios. The interaction with the turbulent and dense northern CSM induces competing effects on electron acceleration: on one hand, turbulence reduces the electron mean free path enhancing the acceleration efficiency, and on the other hand, lower shock velocities increase the acceleration timescale. In most filaments, these effects compensate each other, but in one region, the acceleration timescale exceeds the synchrotron timescale, resulting in a significant decrease in nonthermal X-ray emission from 2006 to 2014, indicating fading synchrotron emission. Our findings provide a coherent understanding of the different regimes of electron acceleration observed in Kepler's SNR through various diagnostics.

Unified Astronomy Thesaurus concepts: Supernova remnants (1667); Interstellar medium (847)

1. Introduction

Supernova remnants (SNRs) are prominent accelerators of particles; thus, they are widely considered the primary origin of galactic cosmic rays. The first observational evidence of very high energy ($E > 10^{12}$ eV) electrons accelerated at SNR shocks was discovered by Koyama et al. (1995), who detected nonthermal X-ray emission stemming from SN 1006 (where efficient hadronic acceleration has also been reported; e.g., Giuffrida et al. 2022). Indeed, the outer shells of young SNRs typically emit synchrotron radiation in the X-ray band, which can be used as a diagnostic tool to deepen our understanding of the acceleration process. The study of X-ray synchrotron emission can provide information about the shape of the electron energy distribution and the mechanisms that limit the maximum energy that electrons can reach (e.g., Miceli et al. 2013).

Kepler's SNR, the aftermath of the explosion of the historical SN 1604, is an interesting object to study the acceleration process in order to study how the environment affects the acceleration mechanism. The remnant, stemming from a Type Ia SN (Kinugasa & Tsunemi 1999), is indeed interacting with a dense nitrogen-rich cloud circumstellar medium (CSM) in the north (Blair et al. 1991, 2007; Reynolds et al. 2007; Katsuda et al. 2008b, 2015; Kasuga et al. 2021). Recent estimates based on proper-motion measurements derived a distance $d = 5.1^{+0.8}_{-0.7}$ kpc (Sankrit et al. 2016). We will adopt $d = 5$ kpc throughout this paper.

Prominent particle acceleration in Kepler's SNR is testified by its energetic nonthermal emission. The presence of nonthermal X-ray emission in Kepler's SNR was first discovered in its southeastern region by Cassam-Chenaï et al. (2004). Recently, Nagayoshi et al. (2021) reported the first strong detection of hard X-ray emission within the 15–30 keV band from Kepler's SNR by analyzing a Suzaku Hard X-ray Detector observation.

In a recent study, Tsuji et al. (2021) analyzed the cutoff photon energy (ε_0) of synchrotron radiation across different regions of several SNRs, including Kepler's SNR. To this end, the authors used a model of synchrotron emission, originally proposed by Zirakashvili & Aharonian (2007), where the electron maximum energy is limited by radiation losses. In this scenario, ε_0 is related to the shock speed, v_{sh}, as

$$\varepsilon_0 = \frac{1.6}{\eta}\left(\frac{v_{sh}}{4000 \text{ km s}^{-1}}\right)^2 \text{keV}, \tag{1}$$

Table 1
Chandra/ACIS Observations Table

ObsID	Exp. Time (ks)	R.A.	Decl.	Start Date
6714	157.8	$17^h30^m42\overset{s}{.}0$	$-21°29'00\overset{''}{.}0$	27/04/2006
6715	159.1	$17^h30^m41\overset{s}{.}2$	$-21°29'31\overset{''}{.}4$	03/08/2006
6716	158.0	$17^h30^m42\overset{s}{.}0$	$-21°29'00\overset{''}{.}0$	05/05/2006
6717	106.8	$17^h30^m41.2$	$-21°29'31.4$	13/07/2006
6718	107.8	$17^h30^m41\overset{s}{.}2$	$-21°29'31.4$	21/07/2006
7366	51.5	$17^h30^m41\overset{s}{.}2$	$-21°29'31\overset{''}{.}4$	16/07/2006
16004	102.7	$17^h30^m41\overset{s}{.}2$	$-21°29'31\overset{''}{.}4$	13/05/2014
16614	36.4	$17^h30^m41\overset{s}{.}2$	$-21°29'31\overset{''}{.}4$	16/05/2014

Figure 1. Chandra/ACIS flux map of Kepler's SNR in the 4.1–6 keV band. The color bar is in a logarithm scale in units of photons cm^{-2} s^{-1}. Source regions are marked with red polygons for the north and white polygons for the south. The background region is marked with the green polygon, and yellow ellipses are the Coffin et al. (2022) point sources used for the astrometric alignment.

where η, or the Bohm factor, is the ratio between the diffusion coefficient and $c\lambda/3$ (where λ is the Larmor radius, the minimum value $\eta = 1$ corresponding to the Bohm limit) and is strongly related to the turbulence of the magnetic field, which scatters the charged particles in the acceleration process. The spatially resolved analysis of Kepler's SNR by Tsuji et al. (2021) lacked the hard part of the spectrum, so no clear correlation between the shock velocity and the synchrotron cutoff energy was found, except for the synchrotron-dominated regions.

In Sapienza et al. (2022), by making use of NuSTAR and XMM-Newton data, we performed a spatially resolved spectral analysis of Kepler's SNR, including the hard part of the X-ray spectrum where the emission is dominated by synchrotron radiation. The spectra were analyzed by adopting the loss-limited model. We identified two different regimes of particle acceleration, characterized by different Bohm factors. In the north, where the shock interacts with a dense CSM, we found a more efficient acceleration (i.e., lower Bohm factor) than in the south, where the shock velocity is higher and there are no signs of shock interaction with dense CSM. This can be explained by considering that the interaction of the shock front with the dense CSM in the north is associated with a turbulent magnetic field, which boosts the particle acceleration process. On the other hand, the low shock speeds measured in the north (Coffin et al. 2022) lead to a high acceleration timescale (∼300 yr), which can result in a decrease of the maximum electron energy by radiation losses. To unravel this intricate scenario on smaller scales, we studied the evolution of the synchrotron flux in several filaments of Kepler's SNR, making use of the two deepest sets of Chandra/ACIS observations performed in 2006 and 2014.

The paper is organized as follows. In Section 2, we present the data sets and the data reduction process, whereas in Section 3, we show the results obtained with the spectral analysis. Discussions and conclusions are drawn, respectively, in Sections 4 and 5.

2. Observation and Data Reduction

For our analysis, we made use of different Chandra/ACIS observations for the two epochs 2006 and 2014, as summarized in Table 1. The data were reprocessed with the CIAO v4.13 software (Fruscione et al. 2006) using CALDB 4.9.4. We reprocessed the data by using the chandra_repro task. We mosaicked flux images for each year by using the merge_obs task. In order to measure proper motion, we followed the same astrometric alignment procedure described by Coffin et al. (2022), selecting the
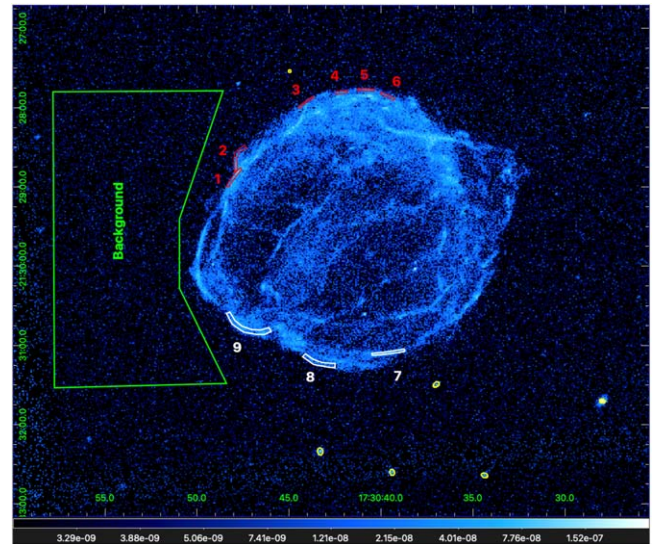
same point sources (also highlighted in yellow in Figure 1). For the proper-motion measurement only, we use the deep 2006 observation (ObsID: 6715) as the relative reference to which we aligned the 2014 deepest observation (ObsID: 16004) in order to minimize systematic errors in the reprojections. To extract spectra, we used specextract CIAO command. We then combined the spectra from the same epochs by using the combine_spectra CIAO command. The spectra were binned using the optimal binning algorithm (Kaastra & Bleeker 2016). The spectral analysis was performed with XSPEC v. 12.11.1 (Arnaud 1996). We adopted the Cash statistic for the fitting procedure.

3. Results

3.1. Spectra

For our spatially resolved spectral analysis, we consider only regions characterized by (i) a bright synchrotron emission, (ii) a sharp edge in the radial distribution of surface brightness (see Bamba et al. 2005), (iii) low contamination from thermal emission, and (iv) at least 1200 photon counts in the spectrum of each epoch (photon counts for all regions are reported in Table 2 for the two epochs). We identify six filamentary regions in the northern part of Kepler's SNR that are clearly visible in the 4.1−6 keV energy band, where the synchrotron radiation dominates the emission, and are located at the rim of the shell. These regions are shown in red in Figure 1 and labeled as 1−6. As a comparison, we also consider three regions in the south (shown in white and labeled as 7−9 in Figure 1).

The source spectra were fitted by adopting the loss-limited model proposed by Zirakashvili & Aharonian (2007) to describe the synchrotron emission and a component from optically thin plasma in nonequilibrium of ionization (vnei) to account for the residual thermal emission (plus two Gaussian components to take into account the missing Fe L line in the model; see Katsuda et al. 2015 and Sapienza et al. 2022). We
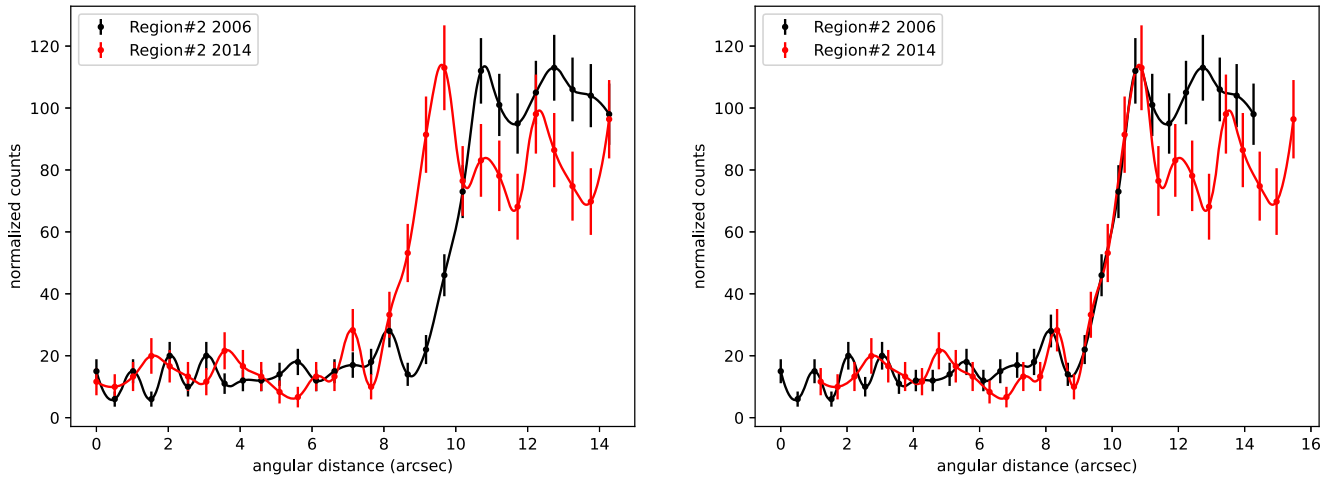
Figure 2. Left panel: example of the one-dimensional radial count profile for region 2 in 2006 (in black) and 2014 (in red). Right panel: same as the left panel but with the 2014 profile shifted according to the procedure described in Williams et al. (2016).

Table 2
Best-fit Parameters for the Regions Shown in Figure 1

Region No.	ε_0 (keV)		Flux 4.1–6 keV ($\log_{10}$ erg cm^{-2} s^{-1})		V_{sh} (km s^{-1})	Counts (0.5–8.0 keV)	
	2006	2014	2006	2014		2006	2014
1	$0.50^{+0.04}_{-0.04}$	$0.9^{+0.3}_{-0.2}$	-13.742 ± 0.014	-13.68 ± 0.03	3570 ± 100	13,023	2072
2	$0.71^{+0.07}_{-0.06}$	$0.80^{+0.23}_{-0.16}$	-13.808 ± 0.014	-13.81 ± 0.03	4690 ± 120	8151	1364
3	$0.40^{+0.07}_{-0.05}$	$0.43^{+0.28}_{-0.14}$	-14.36 ± 0.03	-14.33 ± 0.07	3690 ± 50	13,350	1678
4	$0.34^{+0.04}_{-0.03}$	$0.38^{+0.14}_{-0.09}$	-14.17 ± 0.02	-14.21 ± 0.05	1870 ± 70	8778	1238
5	$0.35^{+0.04}_{-0.04}$	$0.19^{+0.05}_{-0.03}$	-14.19 ± 0.02	-14.42 ± 0.06	1520 ± 100	9824	1494
6	$0.193^{+0.017}_{-0.015}$	$0.25^{+0.06}_{-0.04}$	-14.22 ± 0.02	-14.20 ± 0.06	1590 ± 60	32,217	4861
7	$0.32^{+0.03}_{-0.02}$	$0.51^{+0.16}_{-0.10}$	-13.963 ± 0.018	-13.89 ± 0.04	4160 ± 70	14,717	2246
8	$1.07^{+0.12}_{-0.10}$	$0.89^{+0.24}_{-0.16}$	-13.499 ± 0.011	-13.51 ± 0.03	7690 ± 70	8133	1432
9	$0.43^{+0.04}_{-0.03}$	$0.36^{+0.07}_{-0.05}$	-13.988 ± 0.018	-13.96 ± 0.04	6000 ± 100	15,631	2528

Note. Errors for ε_0 and flux are at the 68% confidence level. Errors for shock velocity are at the 90% confidence level.

modeled the background by a phenomenological fitting of the spectrum extracted from the green region in Figure 1. The background model (properly scaled to account for the different areas of the extraction regions) was then added to the source model. From the best-fit model of each region, we computed the flux in the 4.1−6 keV band by using the `cflux` convolution model.[10] We note that in the 4.1−6 keV band, the flux is dominated by the nonthermal component, whose contribution is always >90% of the total in each region (see also Figures A1 and A2 in the Appendix). The best-fit parameters for 2006 and 2014 are shown in Table 2, while the spectra with the best-fit model and residuals are shown in the Appendix in Figures A1 and A2.

3.2. Shock Velocity Measurement

To estimate the shock velocity, we measured the proper motion from 2006 to 2014 in all nine regions. We mirrored the methodology adopted by Katsuda et al. (2008a), where a deeper description of the procedure can be found. We extract

the one-dimensional radial count profiles of each filament from both the 2006 and 2014 epochs. The profiles were extracted using Chandra/ACIS events file with $0\rlap{.}''492$ per pixel. Each profile was then remapped onto a 40 times denser grid using a quadratic interpolation, in a similar fashion to Williams et al. (2016). The square root of the counts was taken as the statistical uncertainty. We then shifted the 2014 profile relative to the 2006 profile, minimizing the value of χ^2. Figure 2 shows the example of the radial count profiles (for region 2) before and after the shifting procedure. In this paper, we only report the statistical errors, which are the 90% confidence limits resulting from a χ^2 increase $\Delta\chi^2 = 2.706$. Once the best-fit value for the angular shift (θ) is obtained, one can derive the shock velocities for each region (assuming a distance $d = 5$ kpc, as stated in the Introduction). The shock velocities with their uncertainties are also reported in Table 2. The shock velocities displayed in Table 2 exhibit a large dispersion, despite the almost circular appearance of the remnant. Nonetheless, our measurements are in good agreement with previous studies (see Katsuda et al. 2008b and Coffin et al. 2022). Similar velocity dispersions have been observed in other round SNRs, such as SN 1006 (Katsuda et al. 2013; Winkler et al. 2014), RCW 86 (Yamaguchi et al. 2016; Suzuki et al. 2022), and Tycho's SNR (Williams et al. 2016).

---

[10] In the `cflux` model, the normalization of one of the additive models must be fixed to a nonzero value (https://heasarc.gsfc.nasa.gov/xanadu/xspec/manual/node289.html), so we fixed the normalization of the thermal component.
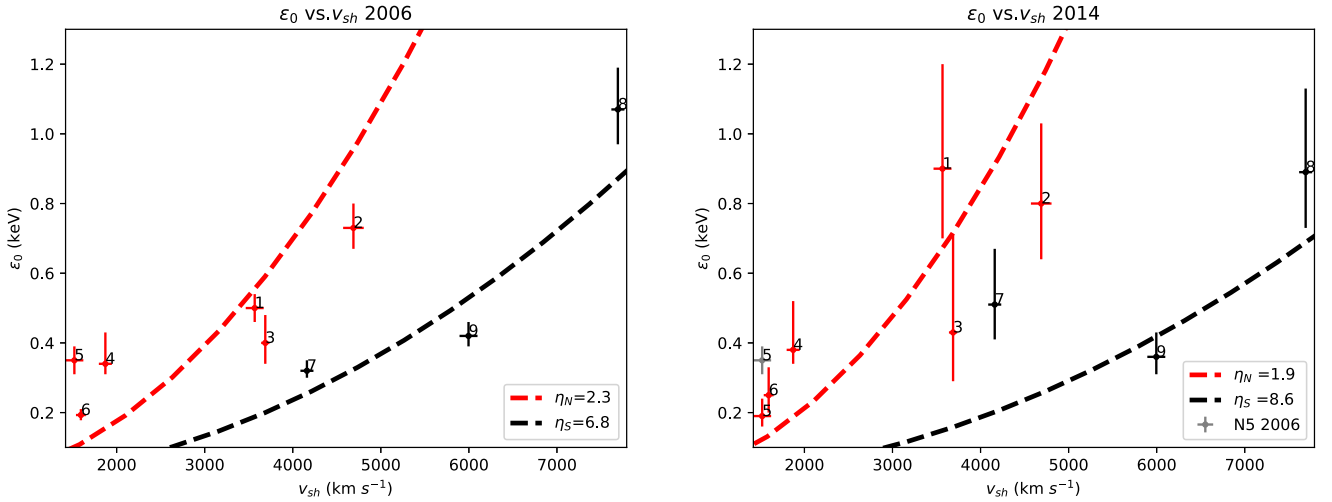
Figure 3. Synchrotron cutoff energy vs. current shock velocity for the year 2006 (left panel) and for the year 2014 (right panel). Red crosses mark northern regions (1–6), and the red dashed curve is the corresponding best-fit curve obtained from Equation (1). Black crosses mark southern regions (7–9), and the black dashed curve is the corresponding best-fit curve obtained from Equation (1). The gray cross in the right panel is region 5 in 2006.

4. Discussion

4.1. Cutoff Photon Energy ε_0 versus the Shock Speed V_{sh}

By employing the same methodology outlined in our previous work, deeply described in Sapienza et al. (2022), we present in Figure 3 the values of ε_0 for the two epochs analyzed, 2006 (left panel) and 2014 (right panel; listed in Table 2), as a function of their corresponding shock velocity ($v_{\rm sh}$). We assumed the same shock velocity for the two epochs. We use different colors to distinguish between data points derived from southern regions (in black) and northern regions (in red). Notably, among all the regions examined, it is only region 5 that shows a significant decline in ε_0 between 2006 and 2014. Figure 3 clearly illustrates the separation of the data points into two distinct clusters (in both epochs), representing the southern and northern regions. This result clearly confirms the existence of two distinct regimes of electron acceleration within the same SNR, already identified by Sapienza et al. (2022). By fitting each of these two clusters using Equation (1), we can derive the corresponding best-fit values of the Bohm factor. For the southern regions, the retrieved Bohm factors are $\eta_S = 6.8 \pm 1.1$ in 2006 and $\overline{\eta}_S = 8.6 \pm 2.0$ in 2014. As for the northern regions, the corresponding Bohm factors are $\eta_N = 2.3 \pm 0.4$ in 2006 and $\overline{\eta}_N = 1{-}3.7$ in 2014. The best-fit values of the Bohm factors align well with those obtained in our previous research (Sapienza et al. 2022), further strengthening the evidence that the electron acceleration proceeds much closer to the Bohm limit in the north than in the south. In particular, $\eta_S/\eta_N = 3.0 \pm 0.7$ and $\overline{\eta}_S/\overline{\eta}_N = 3.6 \pm 2.0$ in 2006 and 2014, respectively.

4.2. Synchrotron Losses versus Acceleration Timescale

Comparing the acceleration time to the synchrotron losses timescale is crucial for determining if the acceleration mechanisms can effectively counteract particle losses, thereby indicating whether the region under investigation follows a loss-limited scenario. The acceleration time of electrons is (Malkov & Drury 2001; Vink 2020)

$$\tau_{\rm acc} \approx 24 \frac{\eta}{\delta} \sqrt{\frac{\varepsilon_0}{1\,{\rm keV}}} \left(\frac{v_{\rm sh}}{5000\,{\rm km\,s^{-1}}}\right)^{-2} \left(\frac{B}{100\,\mu{\rm G}}\right)^{-\frac{3}{2}}\,{\rm yr}, \quad (2)$$
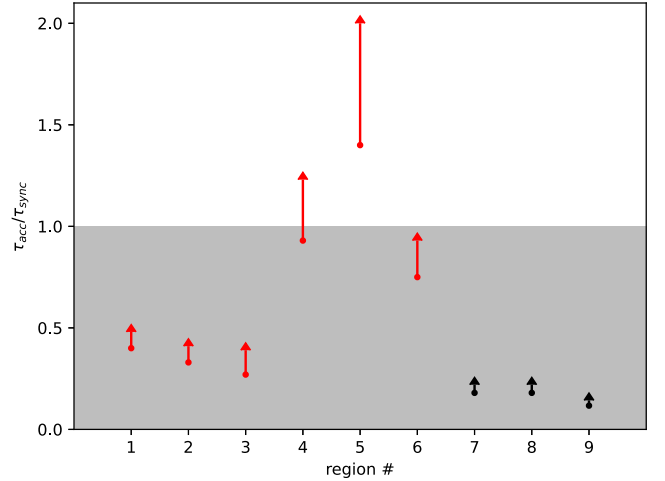

Figure 4. Lower limit of the ratio between the acceleration timescale and the synchrotron losses timescale for the selected region. The arrows indicate the error associated with the lower limit value.

where δ is a parameter that accounts for the energy dependence of the diffusion coefficient, typically ranging between 0.3 and 0.7 (see Strong et al. 2007). Since we assume an energy-independent (and rigidity-independent) Bohm factor, we have $\delta = 1$ by definition for our paper. The synchrotron cooling time is (Longair 1994)

$$\tau_{\rm sync} \approx 55 \left(\frac{\varepsilon_0}{1\,{\rm keV}}\right)^{-1/2} \left(\frac{B}{100\,\mu{\rm G}}\right)^{-3/2}\,{\rm yr}. \quad (3)$$

We can derive the ratio $\tau_{\rm acc}/\tau_{\rm sync}$, which does not depend on the magnetic field but depends on $v_{\rm sh}$, ε_0, η (the Bohm factor), and δ. We estimated the lower limit of the ratio $\tau_{\rm acc}/\tau_{\rm sync}$ for each region by putting $\delta = \eta = 1$ and propagating the errors associated with $v_{\rm sh}$ and ε_0. Results are shown in Figure 4.

The figure shows that, except for region 5, the acceleration timescale at the Bohm limit is always shorter than the synchrotron cooling time; i.e., in these regions, loss-limited conditions ($\tau_{\rm acc}/\tau_{\rm sync} = 1$) can be achieved with $\eta \geqslant 1$. In particular, in agreement with what we have discussed so far,
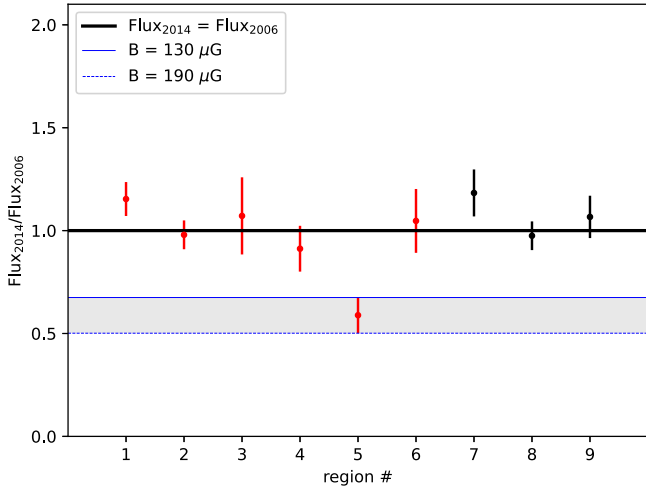
Figure 5. Ratio of the 2014 nonthermal flux (4.1−6 keV) to that measured in 2006 for northern regions (in red) and southern regions (in black). The blue lines represent the theoretical flux decrease expected for synchrotron losses with a magnetic field strength of 130 μG (solid line) and 190 μG (dashed line).

loss-limited conditions are achieved with the values of η_S and η_N reported in Section 4.1 (see also Figure 3). In this case, we expect a steady synchrotron flux and no significant variations between 2006 and 2014.

On the other hand, we find that in region 5, the ratio $\tau_{\rm acc}/\tau_{\rm sync}$ is significantly above the value of 1, whatever the Bohm factor. This means that the acceleration timescale is way longer than the synchrotron cooling time, so the electrons in this region are cooling faster than they are accelerating. We then expect the synchrotron flux of this region to decrease with time. Figure 4 also shows a sort of trend for regions 4, 5, and 6, which exhibit higher ratios compared to other regions. This could be suggestive that these regions may be entering a phase where the acceleration mechanisms are less efficient at counteracting particle losses. Consequently, the synchrotron flux in these regions may decrease over future epochs and might be monitored by future observations.

4.3. Flux Variability

In Figure 5, we illustrate the ratio of the synchrotron flux (4.1−6 keV) in 2014 to that in 2006 for the northern regions (1−6; in red) and the southern regions (7−9; in black). Remarkably, except for region 5, the examined regions in the north do not show any significant decrease in flux. This confirms that these regions have remained within a loss-limited regime throughout the 8 yr time base considered, as predicted in Section 4.2.

Interestingly, the measurements of flux in region 5 show a significant decrease of the synchrotron radiation over this 8 yr baseline. This effect results from the synchrotron losses dominating over the acceleration efficiency, as predicted in Section 4.2 and in nice agreement with what we show in Figure 4. As a further confirmation for this scenario, we show in Figure 5 the comparison of the observed flux decrease with that expected from synchrotron[11] in a magnetic field of 130 and 190 μG (solid and dashed blue curves in Figure 5, respectively), showing the consistency between model and data points.

---

[11] The theoretical decrease of the flux is calculated by numerical integration of the product of the "single-electron" emissivity and the momentum distribution of electrons taking into account their radiative losses in the magnetic field.

Conversely, regions 1 and 7 show a barely significant ($\gtrsim 1\sigma$ level) increase in flux between the two epochs, which may suggest that in these regions, $t_{\rm acc} < t_{\rm syn}$. Further investigations are necessary to confirm this latest point.

4.4. Magnetic Field Strength from Electron Cooling

Figure 5 shows that the flux decrease for region 5 agrees with theoretical predictions for electrons emitting in magnetic fields with strength $B \simeq 130-190\,\mu$G (blue lines). We here suggest another method to estimate B in this region, by considering the decrease of the photon cutoff energy ε_0.

Electrons lose their energy through synchrotron radiation, $\dot{E} = -AB^2E^2$, where $A = 1/637$ in cgs units. By solving this differential equation for the final energy E, we obtain

$$E(t) = \frac{E_{\rm i}}{1 + E_{\rm i}/E_{\rm f}(t)}, \qquad (4)$$

where $E_{\rm i}$ is the initial energy of electrons (at time $t_{\rm i}$), $E_{\rm f} = [AB^2(t - t_{\rm i})]^{-1}$. The radiative losses are effective if the energy $E_{\rm i}$ is about or larger than $E_{\rm f}$. Electrons radiate most of the synchrotron emission in photons with energy $\varepsilon_0 = 0.29 c_2 B E^2$, where $c_2 = 4.2 \times 10^{-8}$ in cgs units. By relating $E_{\rm i}$ and E in Equation (4) to the cutoff energy ε_0 at different times, we have an expression,

$$B = 1450 \left(\frac{\varepsilon_{0,\rm keV}^{-1/2} - \varepsilon_{0i,\rm keV}^{-1/2}}{t_{\rm yr} - t_{\rm i,yr}} \right)^{2/3} \mu{\rm G}, \qquad (5)$$

to estimate the strength of the magnetic field in a region where the photon cutoff energy drops due to the radiative losses. It yields $B = 260 \pm 70\,\mu$G for region 5. This value agrees within the errors with that derived from the flux decrease (refer to Figure 5). The difference in estimation of the magnetic field strength could be due to the spatial orientation of the magnetic field. Indeed, the synchrotron flux reflects the component B in the plane of the sky, while the radiative losses of rapidly isotropized electrons are sensitive to the total B.

We note that Equation (5) assumes that no electrons with energy $\geqslant E$ are supplied by the diffusive shock acceleration. If this is not the case, the estimated value of B should be considered as the lower bound for the magnetic field strength in the region.

4.5. A Comparison with Radio Polarization

The measurement of polarization plays a significant role in SNRs, as it serves as an indicator of the ordering of the magnetic field. Taking advantage of the radio fractional polarization map, we can test the scenario we have proposed for Kepler's SNR.

Figure 6 presents the 1.4 GHz fractional polarization map from DeLaney et al. (2002). In the map, the north shows a polarization fraction that is, on average, lower than in the south. Since a lower value of the polarization fraction is associated with a more turbulent magnetic field, this result is additional proof that points toward a scenario in which the electron acceleration in the north is enhanced by a turbulent magnetic field, generated in the interaction of the shock with the dense CSM.

A similar pattern was found by Suzuki et al. (2022) in RCW 86 (in the southwestern region, where the remnant is interacting
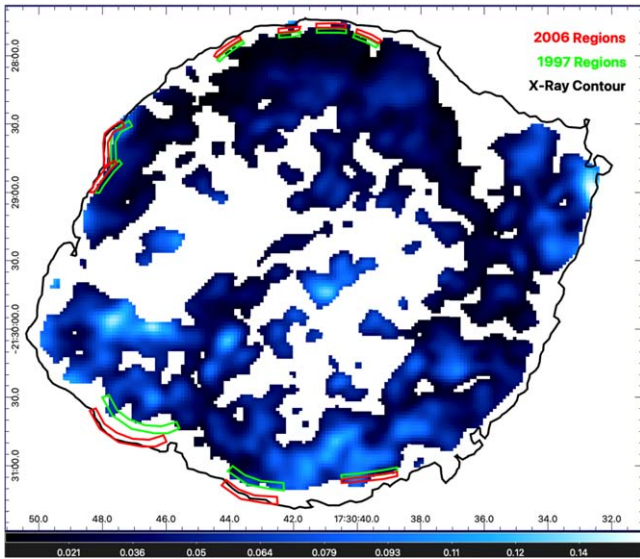
Figure 6. Polarization fraction at 1.4 GHz from DeLaney et al. (2002). The color bar is in linear scale. The black contours overlaid indicate the Chandra/ACIS image for the year 2000. The red polygons are the same as Figure 1. The green polygons are the extraction regions (shifted to take in account the proper motion) to measure the spectral index and polarization fraction.

Table 3
The Radio Index α between 1.4 and 4.8 GHz and the Polarization Fraction Π at 1.4 and 4.8 GHz from the Radio Data of DeLaney et al. (2002)

Region	α	$\Pi_{1.4}$, %	$\Pi_{4.8}$, %
1	0.680 ± 0.009	4.1 ± 0.5	7.3 ± 0.5
2	0.670 ± 0.007	7.4 ± 1.2	13.6 ± 2.7
3	0.690 ± 0.006	2.1 ± 0.2	4.5 ± 0.8
4	0.680 ± 0.002	1.5 ± 0.1	4.6 ± 0.2
5	0.670 ± 0.003	2.7 ± 0.2	3.0 ± 0.7
6	0.680 ± 0.002	1.4 ± 0.2	3.5 ± 0.8
7	0.660 ± 0.019	6.4 ± 2.5	9.0 ± 3.2
8	0.660 ± 0.009	6.2 ± 1.5	5.6 ± 1.4
9	0.690 ± 0.022	5.3 ± 1.5	9.3 ± 2.9

Note. Errors shown are 1σ statistical only.

with a dense cloud). In particular, they retrieved a low Bohm factor in the region where radio observations show a low degree of polarization (Dickel et al. 2001). Sano & Fukui (2021) propose that the observed effect occurs due to not only the density of the CSM but also its clumpiness. Bamba et al. (2023), comparing the southwest rim in RCW 86 of Suzuki et al. (2022) with the northwest rim, which show opposite behaviors, also suggest that this difference may be due to the clumpiness of dense material interacting with the shock.

We calculated the polarization fraction and the radio index from the data of DeLaney et al. (2002) in the nine regions shown in Figure 1. The regions corresponds to regions 1−9 of Figure 1 but are shifted inward to account for the expansion of the SNR in the period between the X-ray and radio observations (which date back to 1997). The measurements are shown in Table 3; the polarization fraction in the north (regions 3–6) is about 3 times smaller than in the south (regions 7–9).

One may use these data for an independent estimate of the difference between the Bohm factor in the north and in the

south for the radio-emitting electrons. Bandiera & Petruk (2016) generalized the classic synchrotron theory to cases where electrons emit in the magnetic field with ordered and disordered components. Equation (31) in this reference relates the radio index and the ratio $\delta B_\perp / B_\perp$ to the polarization fraction (the index $\perp$ refers to the components in the plane of the sky). This relation yields $\delta B_\perp / B_\perp = 4.20 \pm 0.01$ and 2.30 ± 0.14 for the north and south, respectively, for the radio data at 1.4 GHz and 2.9 ± 0.01 and 2.00 ± 0.07 for the data at 4.8 GHz. Next, the relation $\eta \approx (\delta B / B)^{-2}$ may be used to estimate η from $\delta B / B$. In this expression, the strengths of the turbulent δB and of the ordered B components refer to the three-dimensional vectors that are related to the projected ones as $\delta B_\perp = \delta B / \sqrt{3}$, $B_\perp = B \sin \varphi$, with φ being the angle between the line of sight and the vector $\boldsymbol{B}$. We do not know the actual three-dimensional orientation of $\boldsymbol{B}$ in our regions of interest. Therefore, by assuming φ to be the same in all the regions, we derive a ratio between the Bohm parameter of the southern regions (η_S) and the Bohm parameter of the northern regions (η_N) as $\eta_S / \eta_N = 3.3 \pm 0.4$ and 2.2 ± 0.5 for the radio data at 1.4 and 4.8 GHz, respectively. These values correspond within the errors to that obtained from the X-ray data analysis.

The data on polarization fraction reveal that the disordered component δB of the magnetic field is higher than the ordered component B in our regions. Figure 11 of DeLaney et al. (2002) shows that the magnetic field vectors are quite ordered over the whole SNR surface, being mostly aligned with a radial orientation. Such a situation may have a place if the high degree of disorder is on scales that are not resolved by the angular resolution of the radio data we used. Another possibility could be if the turbulence is isotropic and the randomly oriented δB vectors cancel each other out within the regions and relevant lines of sight, leaving the only the ordered component B visible in the polarization vector maps.

5. Conclusions

We analyzed different Chandra/ACIS archive observations of Kepler's SNR in two separate epochs: 2006 and 2014. Our analysis has added some significant findings to our previous study (Sapienza et al. 2022) regarding particle acceleration and synchrotron emission in Kepler's SNR. First, our research has confirmed the existence of two distinct regimes of particle acceleration, with electron acceleration proceeding closer to the Bohm limit in the northern part of the remnant than in the freely expanding southern part. This strongly supports the scenario in which the interaction between the shock and dense CSM in the northern regions results in the amplification of magnetic field turbulence that speeds up the acceleration process. The analysis of the polarization fraction in Kepler's SNR provides further compelling evidence that the acceleration process is influenced by the magnetic field's turbulent nature. The lower polarization fraction observed in the northern region, in fact, suggests the presence of an enhancement of the magnetic field turbulence therein.

While the reduction of the Bohm factor in the north speeds up the acceleration process, the interaction with the dense CSM significantly decelerates the shock, thus increasing the acceleration time. We find that the two effects compensate for each other in the majority of the regions analyzed, and the electron acceleration proceeds steadily in the loss-limited regime. However, in one region (characterized by a very low shock speed), we find that the radiative losses dominate over

the acceleration process, and we report a gradual decrease in the synchrotron emission together with a decrease in the cutoff photon energy.

This provides evidence of a fading synchrotron emission in the northern part of Kepler's SNR, which is in agreement with earlier results by Dickel et al. (1988). The drop of the flux and of the cutoff energy allows us to estimate the local strength of the magnetic field ($B \sim 130-190 \, \mu G$).

Overall, our study provides a coherent and comprehensive understanding of the electron acceleration in Kepler's SNR. The role played by the CSM interacting with the shock in affecting the particle acceleration and synchrotron emission has been elucidated, contributing to a deeper comprehension of this fascinating celestial object.

Acknowledgments

Appendix
Spectra

Figures A1 and A2 show the spectra extracted from the regions in Figure 1 for the years 2006 and 2014, respectively.
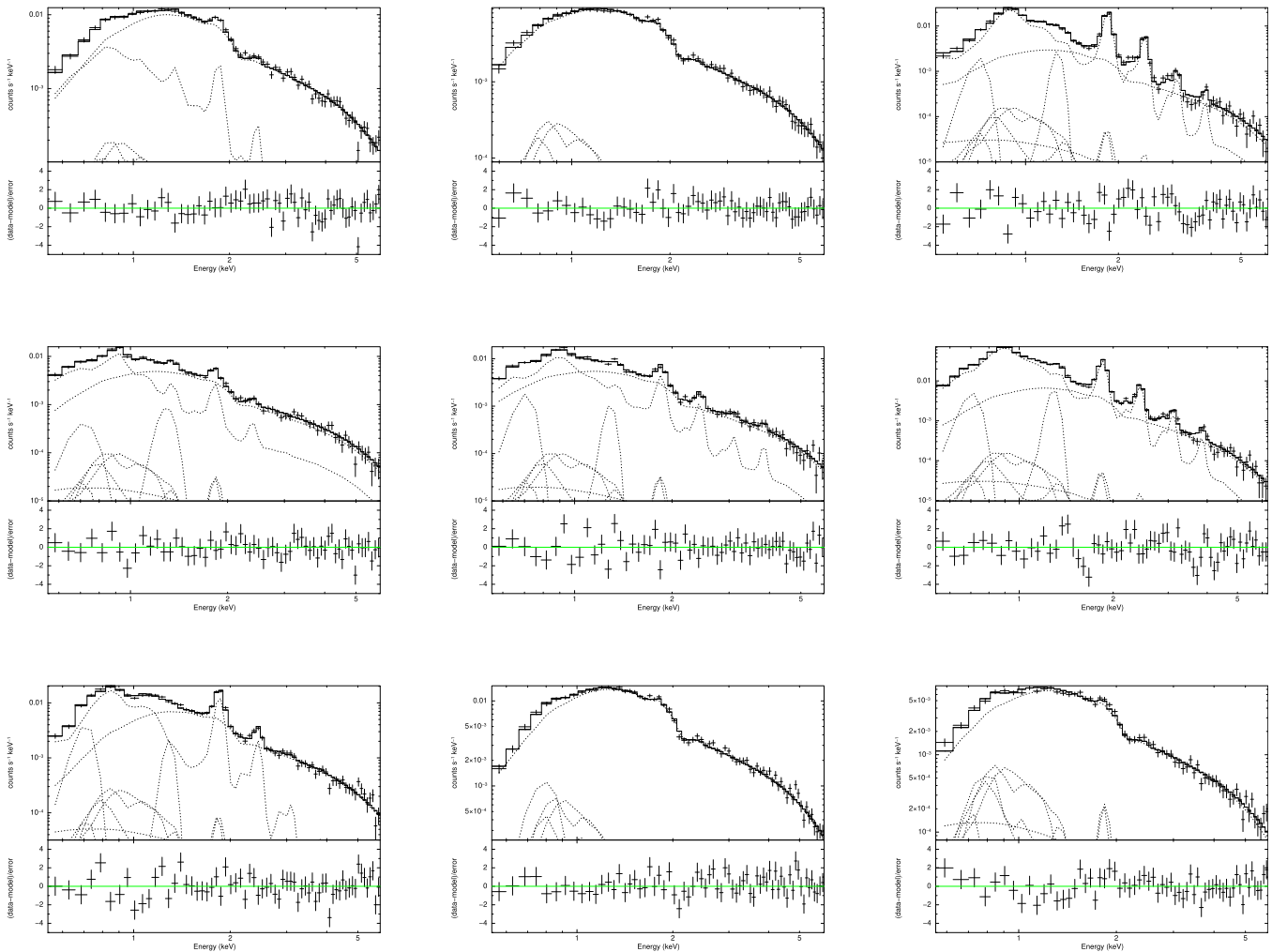

Figure A1. Spectra extracted from the regions in Figure 1 with best-fit models and residuals for the year 2006.
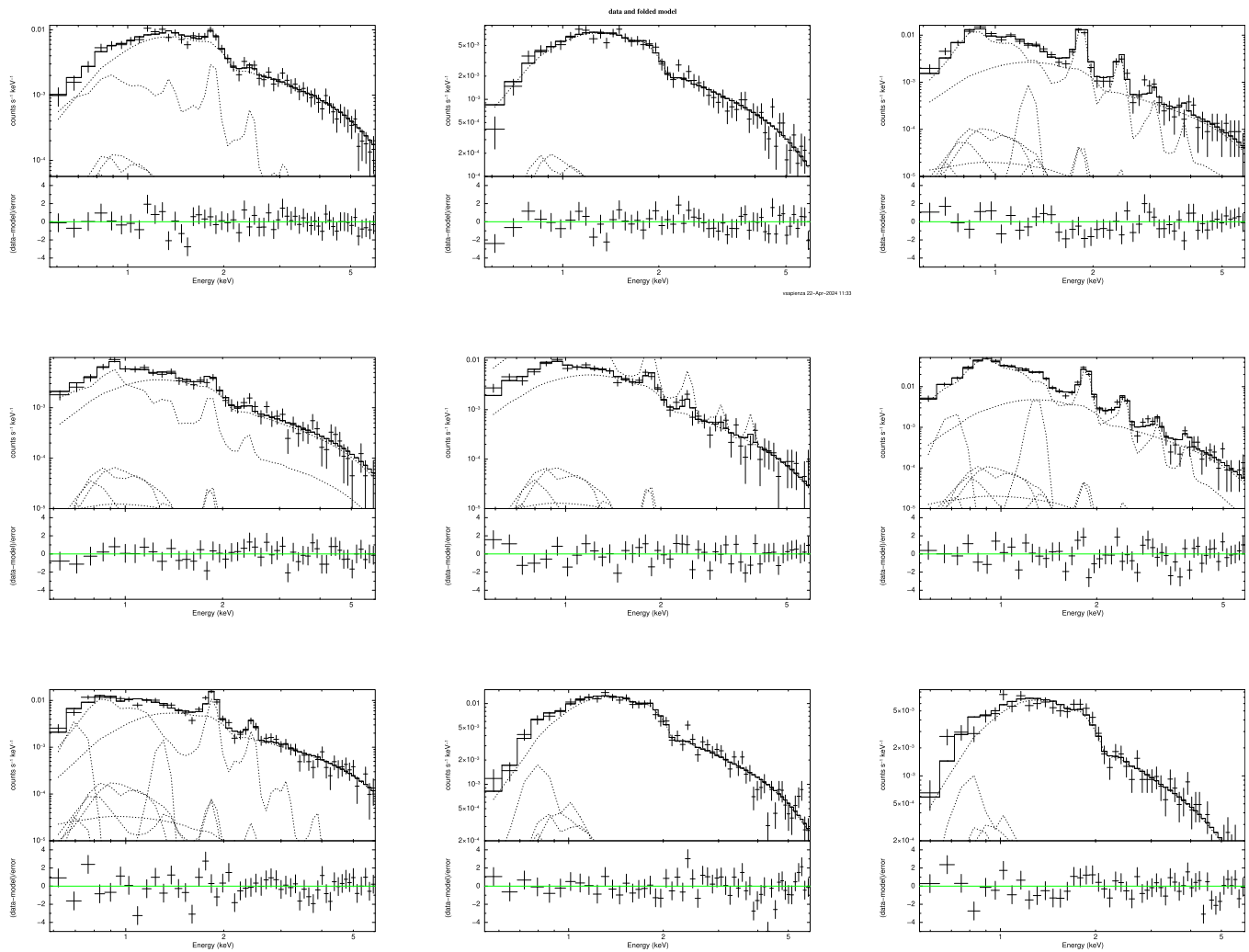
7

Figure A2. Spectra extracted from the regions in Figure 1 with best-fit models and residuals for the year 2014.

ORCID iDs

Vincenzo Sapienza ● https://orcid.org/0000-0002-6045-136X
Marco Miceli ● https://orcid.org/0000-0003-0876-8391
Oleh Petruk ● https://orcid.org/0000-0003-3487-0349
Aya Bamba ● https://orcid.org/0000-0003-0890-4920
Satoru Katsuda ● https://orcid.org/0000-0002-1104-7205
Salvatore Orlando ● https://orcid.org/0000-0003-2836-540X
Fabrizio Bocchino ● https://orcid.org/0000-0002-2321-5616

References

Arnaud, K. A. 1996, in ASP Conf. Ser. 101, Astronomical Data Analysis Software and Systems V, ed. G. H. Jacoby & J. Barnes (San Francisco, CA: ASP), 17
Bamba, A., Sano, H., Yamazaki, R., & Vink, J. 2023, PASJ, 75, 1344
Bamba, A., Yamazaki, R., Yoshida, T., Terasawa, T., & Koyama, K. 2005, ApJ, 621, 793
Bandiera, R., & Petruk, O. 2016, MNRAS, 459, 178
Blair, W. P., Ghavamian, P., Long, K. S., et al. 2007, ApJ, 662, 998
Blair, W. P., Long, K. S., & Vancura, O. 1991, ApJ, 366, 484
Cassam-Chenaï, G., Decourchelle, A., Ballet, J., et al. 2004, A&A, 414, 545
Coffin, S. C., Williams, B. J., & Katsuda, S. 2022, ApJ, 926, 84
DeLaney, T., Koralesky, B., Rudnick, L., & Dickel, J. R. 2002, ApJ, 580, 914
Dickel, J. R., Sault, R., Arendt, R. G., Matsui, Y., & Korista, K. T. 1988, ApJ, 330, 254
Dickel, J. R., Strom, R. G., & Milne, D. K. 2001, ApJ, 546, 447
Fruscione, A., McDowell, J. C., Allen, G. E., et al. 2006, Proc. SPIE, 6270, 62701V

Giuffrida, R., Miceli, M., Caprioli, D., et al. 2022, NatCo, 13, 5098
Kaastra, J. S., & Bleeker, J. A. M. 2016, A&A, 587, A151
Kasuga, T., Vink, J., Katsuda, S., et al. 2021, ApJ, 915, 42
Katsuda, S., Long, K. S., Petre, R., et al. 2013, ApJ, 763, 85
Katsuda, S., Mori, K., Maeda, K., et al. 2015, ApJ, 808, 49
Katsuda, S., Tsunemi, H., & Mori, K. 2008a, ApJL, 678, L35
Katsuda, S., Tsunemi, H., Uchida, H., & Kimura, M. 2008b, ApJ, 689, 225
Kinugasa, K., & Tsunemi, H. 1999, PASJ, 51, 239
Koyama, K., Petre, R., Gotthelf, E. V., et al. 1995, Natur, 378, 255
Longair, M. S. 1994, High Energy Astrophysics: Stars, the Galaxy and the Interstellar Medium, Vol. 2 (Cambridge: Cambridge Univ. Press)
Malkov, M. A., & Drury, L. O. 2001, RPPh, 64, 429
Miceli, M., Bocchino, F., Decourchelle, A., et al. 2013, A&A, 556, A80
Nagayoshi, T., Bamba, A., Katsuda, S., & Terada, Y. 2021, PASJ, 73, 302
Reynolds, S. P., Borkowski, K. J., Hwang, U., et al. 2007, ApJL, 668, L135
Sankrit, R., Raymond, J. C., Blair, W. P., et al. 2016, ApJ, 817, 36
Sano, H., & Fukui, Y. 2021, Ap&SS, 366, 58
Sapienza, V., Miceli, M., Bamba, A., et al. 2022, ApJ, 935, 152
Strong, A. W., Moskalenko, I. V., & Ptuskin, V. S. 2007, ARNPS, 57, 285
Suzuki, H., Katsuda, S., Tanaka, T., et al. 2022, ApJ, 938, 59
Tsuji, N., Uchiyama, Y., Khangulyan, D., & Aharonian, F. 2021, ApJ, 907, 117
Vink, J. 2020, Physics and Evolution of Supernova Remnants (Cham: Springer)
Williams, B. J., Chomiuk, L., Hewitt, J. W., et al. 2016, ApJL, 823, L32
Winkler, P. F., Williams, B. J., Reynolds, S. P., et al. 2014, ApJ, 781, 65
Yamaguchi, H., Katsuda, S., Castro, D., et al. 2016, ApJL, 820, L3
Zirakashvili, V. N., & Aharonian, F. 2007, A&A, 465, 695